ACS APPLIED MATERIALS & INTERFACES

Research Article

Cite This: ACS Appl. Mater. Interfaces 2019, 11, 10651−10662

www.acsami.org

Roles of N-Vacancies over Porous g-C_3N_4 Microtubes during Photocatalytic NO_x Removal

Zhenyu Wang,[†,‡,§] Yu Huang,*[,†,‡] Meijuan Chen,[§] Xianjin Shi,[†,‡] Yufei Zhang,[†,‡] Junji Cao,[†,‡,§] Wingkei Ho,[∥] and Shun Cheng Lee[⊥]

[†]Key Lab of Aerosol Chemistry & Physics, State Key Lab of Loess and Quaternary Geology (SKLLQG), Institute of Earth Environment, Chinese Academy of Sciences (CAS), Xi'an 710061, P. R. China

[‡]CAS Center for Excellence in Quaternary Science and Global Change, Xi'an 710061, P. R. China

[§]School of Human Settlements and Civil Engineering, Xi'an Jiaotong University, Xi'an 710049, P. R. China

[∥]Department of Science and Environmental Studies, The Education University of Hong Kong, Hong Kong, P. R. China

[⊥]Department of Civil and Environmental Engineering, The Hong Kong Polytechnic University, Hong Kong, P. R. China

Supporting Information

ABSTRACT: The development of catalysts that effectively activate target pollutants and promote their complete conversion is an admirable objective in the environmental photocatalysis field. In this work, graphitic carbon nitride (g-C_3N_4) microtubes with tunable N-vacancy concentrations were controllably fabricated using an in situ soft-chemical method. The morphological evolution of g-C_3N_4, from the bulk to the porous tubular architecture, is discussed in detail with the aid of time-resolved hydrothermal experiments. We found that the NO removal ratio and apparent reaction rate constant of the g-C_3N_4 microtubes were 1.8 and 2.6 times higher than those of pristine g-C_3N_4, respectively. By combining detailed experimental characterization and density functional theory calculations, the effects of N-vacancies in the g-C_3N_4 microtubes on O_2 and NO adsorption activation, electron capture, and electronic structure were systematically investigated. These results demonstrate that surface N-vacancies act as specific sites for the adsorption activation of reactants and photoinduced electron capture, while enhancing the light-absorbing capability of g-C_3N_4. Moreover, the porous wall structures of the as-prepared g-C_3N_4 microtubes facilitate the diffusion of reactants, and their tubular architectures favor the oriented transfer of charge carriers. The intermediates formed during photocatalytic NO removal processes were identified by in situ diffuse reflectance infrared Fourier transform spectroscopy, and different reaction pathways over pristine and N-deficient g-C_3N_4 are proposed. This study provides a feasible strategy for air pollution control over g-C_3N_4 by introducing N-vacancy and porous tubular architecture simultaneously.

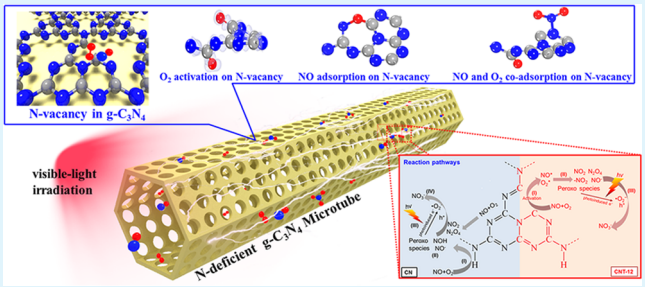

KEYWORDS: *N-vacancy, tubular g-C_3N_4, porosity, photocatalytic NO_x removal*

INTRODUCTION

Nitric oxides (NO_x) are among the most important ozone- and haze-forming precursors.[1,2] Transforming and using solar energy to trigger the photocatalytic removal NO_x under ambient conditions has attracted tremendous attention.[3] Photogenerated active species can oxidize gas-phase NO_x to particulate-phase nitrate, which purifies the air.[4−9] Compared to traditional metallic oxide catalysts (e.g., TiO_2 and $SrTiO_3$), graphitic carbon nitride (g-C_3N_4) with fascinating two-dimensional graphite-like layered structure has received significant attention as a nonmetallic and visible light-responsive photocatalyst for NO_x degradation applications.[10−17] Previous studies have also demonstrated that superoxide ($^{\bullet}O_2^-$) and photogenerated holes (h^+) are the dominant active species employed by g-C_3N_4 to remove NO_x.[11,18,19] Unfortunately, pristine g-C_3N_4, with its irregular bulk morphology, removes NO_x inefficiently. On the one hand, pristine g-C_3N_4, with an intact tri-*s*-triazine structure, shows limited ability to adsorption-activate target reactants (O_2 and NO) and absorbs visible light poorly due to the lack of redundant coordination bonds and defect states in its electronic structure, respectively.[20,21] On the other hand, photogenerated charge carriers diffuse randomly in the bulk g-C_3N_4 due to the lack of an engineered morphology and electron-capture sites, which promotes the recombination of electron−hole pairs.[11,22,23] With the aim of remedying these deficiencies, constructing adsorption activation sites, modifying the electronic structure, and engineering the morphology of g-C_3N_4 are expected to be effective strategies.

Received: December 17, 2018
Accepted: February 26, 2019
Published: February 26, 2019

DOI: 10.1021/acsami.8b21987
ACS Appl. Mater. Interfaces 2019, 11, 10651−10662

Intrinsic anionic vacancies are important for heterogeneous reactions because they improve the light-absorbing abilities of materials while acting as specific sites that adsorption-activate reactant molecules and capture electrons.[24,25] The positive roles of oxygen vacancies (O-vacancies), typical anionic vacancies in oxides, in O_2 activation, electron capture, and the efficient use of incident light have been actively pursued.[26−29] Hence, inspired by findings related to O-vacancy materials, nitrogen vacancies (N-vacancies, typical anionic vacancies in nitrides) in g-C_3N_4 have the potential to effectively activate target pollutants, capture photogenerated charge carriers, and engineer the band structure; however, challenges still remain. Current approaches for introducing N-vacancies into g-C_3N_4 involve calcining processors under different atmospheric conditions or calcining at different temperatures in inert gases;[30,31] however, these approaches cannot engineering the morphology of the material. In addition, the roles of N-vacancies in electronic structure engineering and in accelerating photogenerated charge-carrier separation have been investigated,[32,33] but the effect of the N-vacancy spatial distribution on electron-separation efficiency was ignored. Notably, the adsorption activation behavior of target reactants (O_2 and NO) on N-deficient surfaces has not been investigated.

Recently, the morphology engineering of irregular architectures into one-dimensional (1D) tubular structures has attracted interest in the oriented transfer of charge carriers.[34] One of the pioneering studies in this area reported that the 1D tubular structure of TiO_2 acted as a highway for the oriented transfer of electrons and exhibited superior charge-carrier separation and transport capabilities as a consequence.[35] Therefore, constructing 1D tubular g-C_3N_4 structures that constrain random photogenerated charge-carrier diffusion is feasible. In recent years, calcining rodlike melamine·cyanuric acid (M·CA) complex precursors to produce tubular g-C_3N_4 has been regarded as a simple and reliable method because it avoids tedious steps and the introduction of impurities. The rodlike precursor of supramolecular M·CA is fabricated by mixing equal amounts of melamine and cyanuric acid, followed by heating at 180 °C.[36,37] Melamine is well known to spontaneously transform into cyanuric acid under suitable conditions. Expensive cyanuric acid is avoided if monomeric melamine is used to fabricate supramolecular M·CA in an in situ self-conversion process. To date, the easy transfer of electrons in the longitudinal direction of tubular g-C_3N_4 has been widely confirmed; however, charge-carrier separation efficiency remains unsatisfactory unless g-C_3N_4 is doped with foreign atoms or by constructing isotypical heterostructures.[38−40] In addition, the enhancement of reactant diffusion is another important function of morphology engineering, and the formation of porous structures is an effective strategy to achieve this. In our previous work, we fabricated honeycomb-like g-C_3N_4 that exhibited improved NO_x-diffusion abilities compared to pristine g-C_3N_4.[41] Therefore, the preparation of porous g-C_3N_4 with a 1D tubular architecture is highly desirable and is expected to accelerate the simultaneous oriented transfer of photoinduced e^-−h^+ pairs, as well as reactant diffusion.

In this work, a series of g-C_3N_4 microtubes with tunable N-vacancy concentrations and porous wall structures were synthesized by an in situ soft-chemical method. The novel synthesis involved calcining N-deficient rodlike precursors, which were synthesized by the self-conversion of monomeric melamine for different hydrothermal treatment times. The morphological evolution of the porous tubular architecture is discussed in detail, aided by time-resolved hydrothermal experiments. The prepared porous g-C_3N_4 microtubes exhibited clearly improved photocatalytic activity for NO_x degradation compared to bulk g-C_3N_4. The effects of N-vacancies on O_2 and NO adsorption activation, electron capture, and electronic structure and the effect of the tubular structure on oriented electron transfer were systematically investigated through experimental and computational studies, which led to the proposal of a mechanism for the enhanced NO removal activity. Furthermore, the reaction pathways for photocatalytic NO removal over pristine g-C_3N_4 and N-deficient g-C_3N_4 were identified by diffuse reflectance infrared Fourier transform spectroscopy (DRIFTS), and a mechanism for photocatalytic NO removal is proposed. This study provides a feasible strategy for air pollution control over g-C_3N_4 by introducing N-vacancy and porous tubular architecture simultaneously.

MATERIALS AND METHODS

Synthesis of Porous g-C_3N_4 Microtubes with Various N-Vacancy Concentrations. Synthetic materials for g-C_3N_4 and other related chemicals were bought from Shanghai Aladdin Bio-Chem Technology Co., Ltd. All chemicals were used without further purification. First, 1 g of melamine was added to 70 mL of deionized water and then the suspension liquid was heated to 60 °C in a water bath kettle with vigorous stirring until dissolution. Then, the obtained solution was transferred into a 100 mL Teflon-lined autoclave and heated at 180 °C for 6, 7, 8, 12, or 16 h; the precursors prepared in this matter are designated as M-6, M-7, M-8, M-12, and M-16, respectively. The hydrothermal products were filtered and washed with deionized water and absolute ethanol three times and subsequently dried at 60 °C for 12 h. Finally, 1 g of M-8, M-12, and M-16 were separately calcined to 550 °C in a muffle furnace for 3 h under a flow of nitrogen (2.5 °C/min); the resulting materials are designated as CNT-8, CNT-12, and CNT-16, respectively. For comparison, pristine g-C_3N_4 (designated as CN) was synthesized by directly calcining 1 g of the precursor prepared by drying solution A at 60 °C.

Characterization. X-ray diffraction (XRD) of the samples was conducted on an X'Pert PRO X-ray diffractometer using Cu Kα radiation (PANalytical, U.K., 2θ scan rate = 0.05°/s, λ = 1.5406 Å, 40 kV, 40 mA). Elemental compositions of the samples were performed on an Elementar Vario EL instrument (Vario EL III, Germany; detection limit, 0.015%; standard deviation, ≤0.1% abs). Fourier transform infrared (FT-IR) spectroscopy of all samples was conducted on a VERTEX 70 FT-IR spectrometer (Bruker, Germany). The surface elemental compositions and states of the samples were conducted on an ESCALAB 250 X-ray photoelectron spectrometer (XPS) (Thermo Fisher). All binding energies were calibrated against the C 1s peak (284.6 eV), which arises from surface adventitious carbon. The morphologies of the samples were examined by scanning electron microscopy (SEM, JEOL JSM-6490, Japan) and transmission electron microscopy (TEM, JEOL JEM-2100HR CM-120, Japan). The Brunauer−Emmett−Teller (BET) surface areas of samples were recorded on an ASAP 2020 nitrogen adsorption analyzer (Micromeritics); the samples were degassed at 250 °C prior to analysis. The free radicals were detected by sample trapping with a 25 mM solution of 5,5′-dimethyl-1-pyrroline-*N*-oxide (DMPO) on an ER200-SRC electron spin resonance (ESR) spectrometer (Bruker, Germany) at low temperature (130 K); aqueous dispersions were used for DMPO−$^{\bullet}$OH, and alcohol dispersions for DMPO−$^{\bullet}O_2^-$. The UV−vis absorption spectra of the samples were recorded on a Varian Cary 100 Scan UV−visible spectrophotometer (Agilent, Australia). The intermediate and final products were detected using ion chromatography (IC) on a Dionex-600 Ion Chromatograph (Dionex Inc.,

DOI: 10.1021/acsami.8b21987
ACS Appl. Mater. Interfaces 2019, 11, 10651−10662

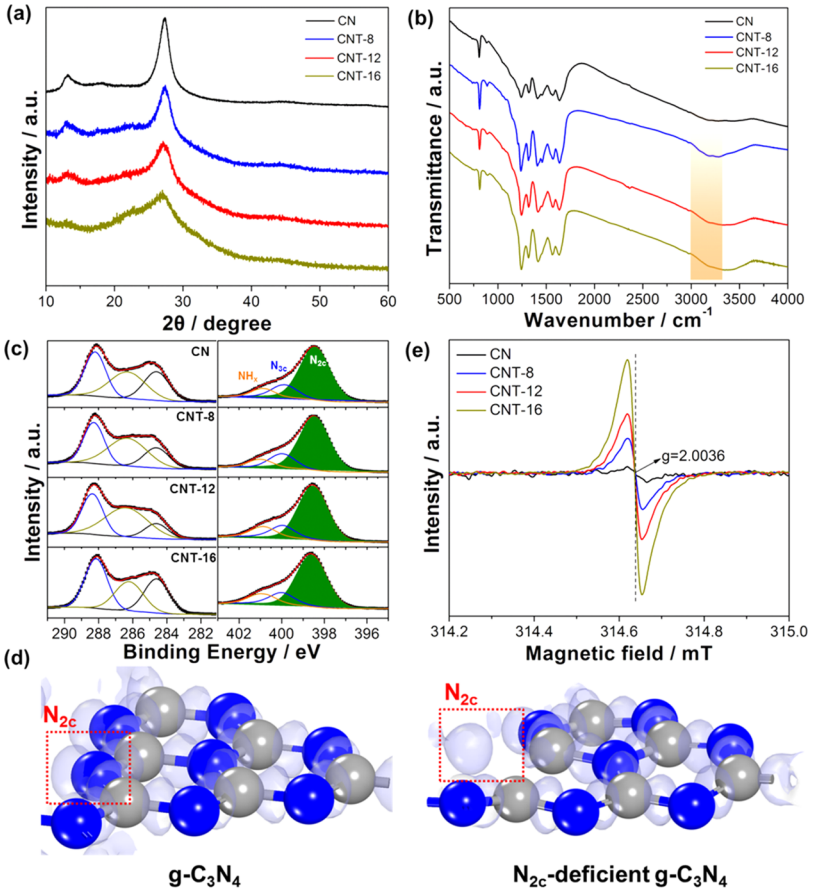

Figure 1. (a) XRD patterns, and (b) FT-IR, (c) high-resolution C 1s and N 1s XPS, and (e) ESR spectra of CN, CNT-8, CNT-12, and CNT-16. (d) Calculated EDD diagrams of g-C_3N_4 (left) and N_{2c}-deficient g-C_3N_4 (right).

Sunnyvale, CA) fitted with an IonPac AS14A column. Photoluminescence (PL) spectra were acquired on an FLS980 fluorescence spectrophotometer (Edinburgh, U.K.).

Computational Modeling. Density functional theory (DFT) calculations were made using the Cambridge Sequential Total Energy Package (CASTEP) software package. The plane-wave basis sets were used to treat valence electrons, while norm-conserving pseudopotentials were used to approximate the potential field.[42,43] A model of the g-C_3N_4 crystal was built through cleavage of the (001) lattice plane, followed by the construction of a 10 Å vacuum slab crystal, as shown in Figure S1a. The g-C_3N_4 crystal model with N-vacancy was constructed by removing a two-coordinated nitrogen atom (Figure S1b). The exchange−correlation Perdew−Burke−Ernzerhof functional was implemented to describe the exchange−correlation energy and electron interactions.[44] The Brillouin zone was separately sampled at 4 × 4 × 1 Monkhorst−Pack *k*-points.[45] A plane-wave cutoff was set to 380 eV for all of the calculations. During geometry optimization, the convergence criterion was set to 1.0 e^{-6} eV/atom for energy, and 0.05 eV/Å for residual force. The electron density difference (EDD) and Mulliken population analysis were used to calculate charge-transfer quantity.[46]

The O_2 and NO adsorption energies (ΔE_{ads}) for the model g-C_3N_4 crystal without and with N-vacancy were calculated using eqs 1 and 2

$$\Delta E_{ads} = E_{O_2+C_3N_4} - E_{O_2} - E_{C_3N_4} \quad (1)$$

$$\Delta E_{ads} = E_{NO+C_3N_4} - E_{NO} - E_{C_3N_4} \quad (2)$$

where ΔE_{ads} is the O_2 or NO adsorption energy, $E_{O_2+C_3N_4}$ and $E_{NO+C_3N_4}$ are the total energies of the model g-C_3N_4 crystal with molecular O_2 and NO adsorbed on its surface, respectively, $\Delta E_{C_3N_4}$ is the total energy of the model pure g-C_3N_4 crystal, E_{O_2} is the energy (−869.17 eV) of molecular O_2 in the gas phase, and E_{NO} is the energy (−705.07 eV) of molecular NO in the gas phase.

Photocatalytic Activity Experiments. The photocatalytic activities of the as-prepared samples toward NO_x removal were conducted in a continuous-flow reactor system. The as-prepared samples (0.1 g) were coated onto a 10.0 cm diameter vitreous culture dish and then placed in a 4.5 L (30 cm × 15 cm × 10 cm) rectangular reactor. The initial NO gas was supplied from a compressed gas cylinder (48 ppm N_2 balance) and diluted to 400 ppb by a zero air generator (Model 1001, Sabio Instruments Inc., Georgetown, TX). A 300 W commercial Xe arc lamp (Perfectlight, China) fitted with a UV cutoff filter was placed vertically outside the reactor and turned on following NO adsorption−desorption equilibrium. The optical power density at the sample surface was calibrated to be 25.28 mW/cm^2 using an optical power meter (Thorlabs PM100D, Newton, NJ). The change of NO_x concentrations was recorded online on a Model 42c chemiluminescence NO analyzer (Thermo Environmental Instruments Inc., Franklin, MA). The removal ratio (η) of NO was calculated as η (%) = $(1 - C/C_0) \times 100$, where C and C_0 are the concentrations of NO in the outlet and feed streams, respectively.

Photoelectrochemical Measurements. The photoelectrochemical experiments were evaluated using a Parstat 4000 electrochemical workstation fitted with three-electrode cell configuration: platinum plate electrode is the counter electrode and the Ag/AgCl electrode is the reference electrode; the as-prepared sample was coated on indium tin oxide substrate and used as the working electrode. For the transient photocurrent measurement, the Na_2SO_3 solution (0.5 mol/L) served as the electrolyte and the photocurrent−time curves were measured at 0.2 V vs Ag/AgCl at ambient temperature under a periodic visible light illumination (Xe lamp, 300 W, Perfectlight, China). For the electrochemical impedance spectroscopy (EIS) measurement, the working electrode was immersed in a 1 mmol/L

DOI: 10.1021/acsami.8b21987
ACS Appl. Mater. Interfaces 2019, 11, 10651−10662

$K_3Fe(CN)_6$ and $K_4Fe(CN)_6$ solution and subjected to 5 mV voltage amplitude in the frequency range of 0.1 Hz to 100 kHz.

In Situ DRIFTS for NO Adsorption−Oxidation. The DRIFTS measurement was performed on a VERTEX 70 FT-IR spectrometer (Bruker, Germany) fitted with a Harrick in situ diffuse reflectance cell and a high-sensitivity mercury cadmium telluride detector. The as-prepared sample was preheated in helium at 250 °C for 45 min to remove surface adsorbates. After cooling to room temperature, the background measurement was conducted. Then, a gas mixture (40% NO and 60% O_2) was fed into the reaction chamber with a total flow of 50 mL/min. After 20 min, visible light was introduced into the reaction chamber and removed after 30 min.

RESULTS AND DISCUSSION

Phase Structures, Chemical Components, and N-Vacancy Analyses. The phase structures of CN, and the CNT-8, CNT-12, and CNT-16 series of samples were investigated by XRD. As shown in Figure 1a, the CN sample exhibits two typical diffraction peaks at 13.2 and 27.3°; the former is assigned to intralayer long-range-ordered tri-*s*-triazine units (100), and the latter is assigned to periodic stacking (002) of layers along the *c*-axis.[13] The (100) peak gradually decreases in intensity in moving to CNT-8 and CNT-12 and is almost absent in the spectrum of CNT-16, which is suggestive of the progressive loss of the periodic structure of the tri-*s*-triazine framework. To further identify the structural defects in the bulk phases of CNT-8, 12, and 16, these materials were first subjected to elemental analysis. The N and C contents of the precursors and prepared g-C_3N_4 are listed in Table S1, with the calculated N/C atomic ratios summarized in Table S2. The N/C atomic ratio was observed to decrease from 2.057 for pristine precursor M to 1.537 for M-16, while the N/C atomic ratios of the g-C_3N_4 samples were determined to be 1.521 for CN, and 1.504, 1.489, and 1.427 for CNT-8, CNT-12, and CNT-16, respectively. The decreasing N content is consistent with the introduction of N-vacancies that destroy the ordered in-plane structure, leading to the gradual disappearance of the (100) peak. Compared to the CN sample, there were 1.1, 2.1, and 6.2 atom % less nitrogen in CNT-8, CNT-12, and CNT-16, respectively. In addition, compared to CN, the (002) peaks of the as-prepared CNT samples gradually weakened and broadened, which is suggestive of a reduced crystal size. In Figure 1b, the FT-IR spectrum of CN exhibits typical bands at 810 cm^{-1} for the breathing mode of the heptazine ring system. The broad 1200−1600 cm^{-1} regions correspond to the stretching vibrations of the C_6N_7 units.[47] The broad 3000−3600 cm^{-1} regions (shaded in orange) correspond to the stretching vibrations of N−H.[48] The remaining CNT samples exhibit distinctly enhanced peaks in the orange shaded regions, which are suggestive of a gradual increase in the concentration of N−H groups, which results in the loss of the in-plane periodicity of the tri-*s*-triazine framework.

The surface elemental compositions and states of the as-prepared samples were further investigated using XPS. Figure 1c reveals that CN exhibits three C 1s peaks around 284.6, 286.3, and 288.2 eV, which correspond to adventitious C−C, C−NH/NH_2, and N−C=N bonds (Table S3).[33,49,50] N 1s peaks are observed around 398.5, 400.0, and 401.0 eV, which are assigned to two-coordinated (N_{2c}) and three-coordinated (N_{3c}) nitrogen atoms, and NH_x groups (Table S3), respectively.[33,49,51] The N/C atomic ratios on the sample surfaces were calculated and found to reveal a decreasing trend, from 1.361 for CN, to 1.322 for CNT-8, 1.299 for CNT-12, and 1.244 for CNT-16 (Table S2), consistent with a gradual increase in the N-vacancy concentration. In addition, the N_{2c}/N_{3c} peak-area ratio was observed to decrease, from 4.92 for CN to 4.72, 4.46, and 4.37 for CNT-8, CNT-12, and CNT-16, respectively (Table S2), indicating that N_{2c} atoms are preferentially lost. The preferential loss of N_{2c} atoms over N_{3c} atoms is attributed to their unsaturated coordinations; original charge balances no longer exist with N_{2c} atoms missing. To illustrate the charge redistribution, the EDDs of g-C_3N_4 and N_{2c}-deficient g-C_3N_4 were calculated by DFT, the results of which are shown in Figure 1d. The N atom at the N_{2c} site obtains 0.39 electrons from its neighboring C atoms in pure g-C_3N_4 (Figure 1d, left). After removal of the N_{2c} atom, the density of the electron cloud increased to 0.52 electrons due to the lack of an electron acceptor (Figure 1d, right). The oxygen concentrations of CN, CNT-8, CNT-12, and CNT-16 were analyzed, and the results are listed in Table S4. From the results of Table S4 and high-resolution O 1s XPS (Figure S2), the low concentrations of oxygens (2.13 atom % for CN, 0.97 atom % for CNT-8, 1.62 atom % for CNT-12, 1.14 atom % for CNT-16) of all of the samples were from the surface-adsorbed water.[33]

The relationship between unpaired electron variation and N-vacancy concentration was further probed by ESR spectroscopy. As shown in Figure 1e, CN exhibits an insignificant single-line ESR signal at a *g*-value near 2.0036, which suggests that there are few localized unpaired electrons present in pristine CN.[21] However, increasing spin intensities were observed for the CNT samples, consistent with a gradual increase in the N-vacancy concentration in moving to CNT-8, CNT-12, and CNT-16.

Morphologies and Formation Mechanism of Porous g-C_3N_4 Microtubes. The morphologies of representative samples were examined by SEM and TEM. As shown in Figure 2a−c, the SEM images of CNT-8, CNT-12, and CNT-16 exhibit similar open-ended tubular structures that are more than 10 μm long and about 3 μm wide, which is distinctly different from that of the CN obtained by calcining melamine directly (Figure S3a). TEM further confirmed that hollow tubular structures were successfully produced. The thickness of the tube wall gradually decreased on moving to CNT-8 (Figure S3b), CNT-12 (Figure 2d), and CNT-16 (Figure S3c). A magnified image of the tube wall of CNT-12 (Figure 2e) shows a large number of 20−50 nm nanopores embedded in the lamellar tube wall. These porous structures are formed in the tube walls in association with gases released during pyrolysis condensation. These porous surfaces facilitate the diffusion of reactants during heterogeneous reactions.[41,52] The SEM and TEM results demonstrate that the in situ soft-chemical method is an effective approach for the construction of the porous tubular structure of g-C_3N_4. The textural properties of these g-C_3N_4 samples were further investigated by acquiring their nitrogen adsorption−desorption isotherms and Barrett−Joyner−Halenda pore size distributions. The specific surface areas of CN, CNT-8, CNT-12, and CNT-16 were found to be 19.9, 28.2, 67.5, and 69.2 m^2/g, respectively (Figure 2f). In addition, the 2−4 nm pore size distribution of CN reflects the porosity within its nanoscale sheets, while the distribution observed at 20−50 nm is attributed to layer-stacked pores. The CNT samples clearly exhibit higher-intensity distribution peaks in these regions due to the effects of layer exfoliation and pore formation, respectively, as evidenced by TEM. Hence, compared to CN, the increased specific surface areas of the

DOI: 10.1021/acsami.8b21987
ACS Appl. Mater. Interfaces 2019, 11, 10651−10662

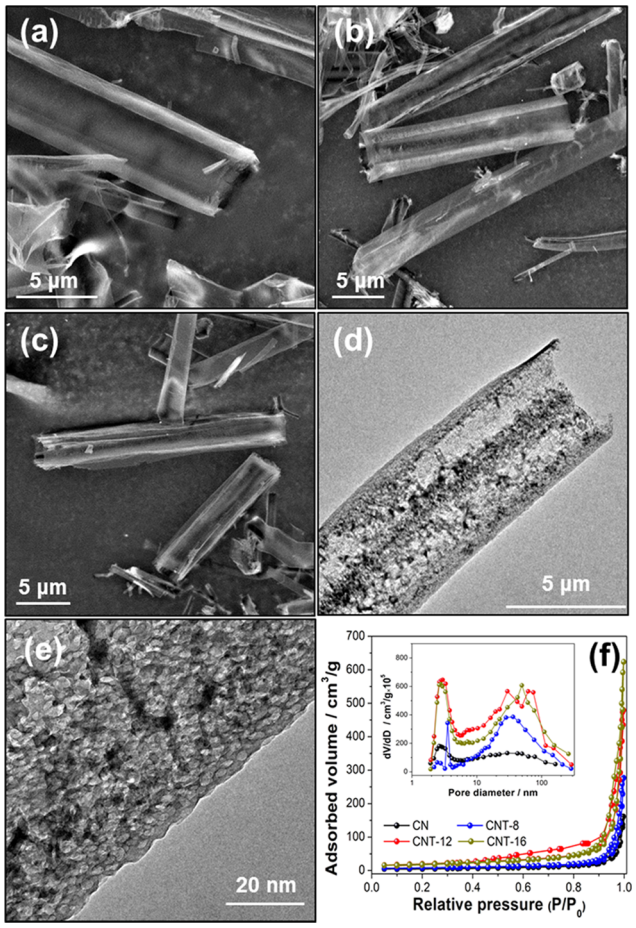

Figure 2. SEM images of (a) CNT-8, (b) CNT-12, and (c) CNT-16. (d) TEM image of CNT-12. (e) Enlarged TEM image of the tubular wall of CNT-12. (f) N_2 adsorption−desorption isotherms of CN, CNT-8, CNT-12, and CNT-16 and the corresponding pore size distribution curves.

CNT samples are attributable to the introduction of porous tubular structures.

The morphological evolution of tubular g-C_3N_4, taking CNT-12 as an example, is displayed through a time-resolved hydrothermal experiment, as shown in Scheme 1. Simply, bulk pristine melamine exhibits an irregular appearance (Figure S4a and Scheme 1,I) and a monoclinic crystal structure (Figure S4d,e).[53] Melamine retains its bulk structure after hydrothermally reacting at 180 °C for 6 h, but its (102) crystal faces are exposed for growth (Figure S4b,d and Scheme 1,II). At a hydrothermal reaction time of 7 h, both bulk and rodlike crystal structures coexist in M-7 (Figure S4c and Scheme 1,III). These new rodlike structures are M·CA supramolecular structures (Figure S4d,g), suggesting that: (1) M was partly converted into CA in situ and (2) the remaining M aggregated with CA to form M·CA supramolecular structures through hydrogen bonding (N−H···O and N−H···N, Scheme 1,III) (changes in the surface functional groups were investigated by FT-IR spectroscopy, as shown in Figure S5, with the corresponding details available in the Supporting Information).[54] At 12 h, hexagonal prismlike rod structures dominate the precursor (Scheme 1,IV). The hydrothermal reaction facilitates rapid precursor recrystallization at the center of each hexagonal rod, resulting in a higher density of defects than in epitaxial growth regions.[39] Hence, after calcining under N_2, pyrolysis-induced collapse occurs from the center of each hexagonal rod in the direction of the tube wall, to form a prismlike hollow tubular g-C_3N_4. Large amounts of NH_3 are released during pyrolysis condensation, which subsequently act as bubble templates that result in abundant pores in the lamellar tube wall (Scheme 1,V).

Evaluating Photocatalytic Activity and Identifying Reactive Species. The photocatalytic degradation of NO under visible light irradiation was examined in a continuous reactor, the results of which are shown in Figure 3a. NO adsorption equilibrium in the dark and reactivity in the absence of a photocatalyst under visible light irradiation were excluded through control experiments. The NO removal ratios (η) over the tubular g-C_3N_4 samples are higher than that of bulk g-C_3N_4. Among them, CNT-12 shows the highest value of η (32.8%) when irradiated by visible light, which is 1.4, 1.2, and 1.8 times higher than those of CNT-8 (23.7%), CNT-16 (26.9%), and CN (18.2%), respectively.

The Langmuir−Hinshelwood model was used to describe the NO photodegradation rates because the initial photocatalytic degradation of NO approximately follows mass-transfer-controlled pseudo-first-order kinetics.[55−57] (The Langmuir−Hinshelwood model is detailed in the Supporting Information along with calculations of apparent rate constant, k.) The apparent reaction rate constant k of CNT-12 (0.045 min^{-1}) was determined to be 2.6, 1.2, and 2.1 times higher than those of CN (0.017 min^{-1}), CNT-8 (0.037 min^{-1}), and CNT-16 (0.021 min^{-1}), respectively (Figure S6). NO_2, as the reaction intermediate, hinders NO degradation because it occupies active sites. Hence, a byproduct of NO_2 is monitored online (Figure S7a), with selectivity subsequently calculated. The results show that CNT-12 displays the lowest conversion ratio of NO to NO_2 among the materials examined, as shown in Figure S7b. After a single run, the accumulated products on the surfaces of the CN and CNT-12 samples were extracted with deionized water and examined by ion chromatography (IC), which revealed that the amounts of NO_3^- and NO_2^- accumulated on the CN surface were 146.7251 and 30.1789 μg/g, respectively, while those accumulated on the CNT-12 surface were 237.6047 and 6.5573 μg/g, respectively. In addition, to further examine photocatalytic stability and durability, CNT-12 was subjected to five cycles of use; the NO removal capability of this material exhibited excellent reproducibility, as shown in Figure 3b.

Spin-trap ESR spectroscopy was performed to identify the active radicals involved during NO removal over CNT-12. As shown in Figure 3c,b, no ESR signals corresponding to $^{\bullet}O_2^-$ and $^{\bullet}OH$ were observed in the dark at the commencement of irradiation. However, after 10 min of visible light irradiation, signals for these two radicals were clearly observed. The observation that the photogenerated holes of CNT-12 are unable to directly oxidize H_2O to active $^{\bullet}OH$ species because the E_{VB} of CNT-12 (1.62 V, the band structures of all samples were determined by UV−vis diffuse reflectance spectroscopy, as detailed in the Supporting Information) is lower than $H_2O/^{\bullet}OH$ (2.37 V) indicates that a proportion of $^{\bullet}O_2^-$ is transformed into $^{\bullet}OH$ radicals via the $^{\bullet}O_2^- \rightarrow H_2O_2 \rightarrow {}^{\bullet}OH$ route.[19] Consequently, signals corresponding to the DMPO−$^{\bullet}OH$ adduct are weaker than those of the DMPO−$^{\bullet}O_2^-$ adduct. Furthermore, the observation that the E_{VB} of CNT-12 is higher than that of HNO_3/NO (0.94 V) implies that holes are able to remove NO by direct oxidation.[58] The following hole scavenger test (detailed in the Supporting

DOI: 10.1021/acsami.8b21987
ACS Appl. Mater. Interfaces 2019, 11, 10651−10662

Scheme 1. Schematic Representation of the Morphological Evolution of CNT-12

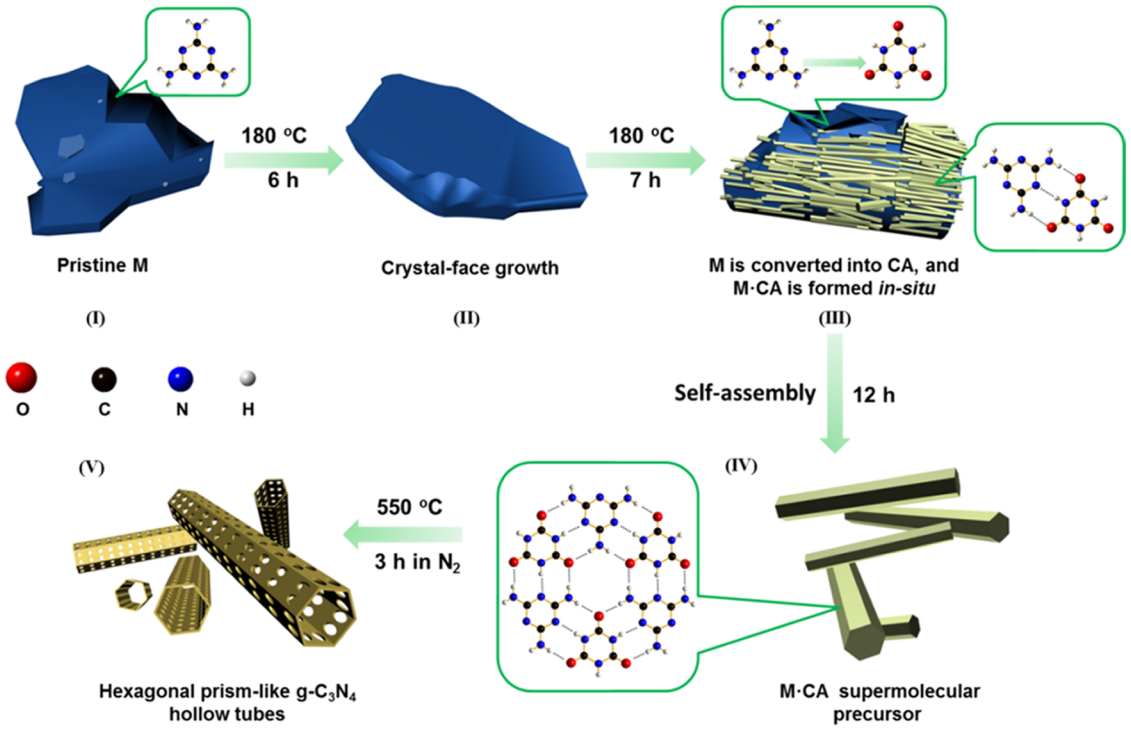

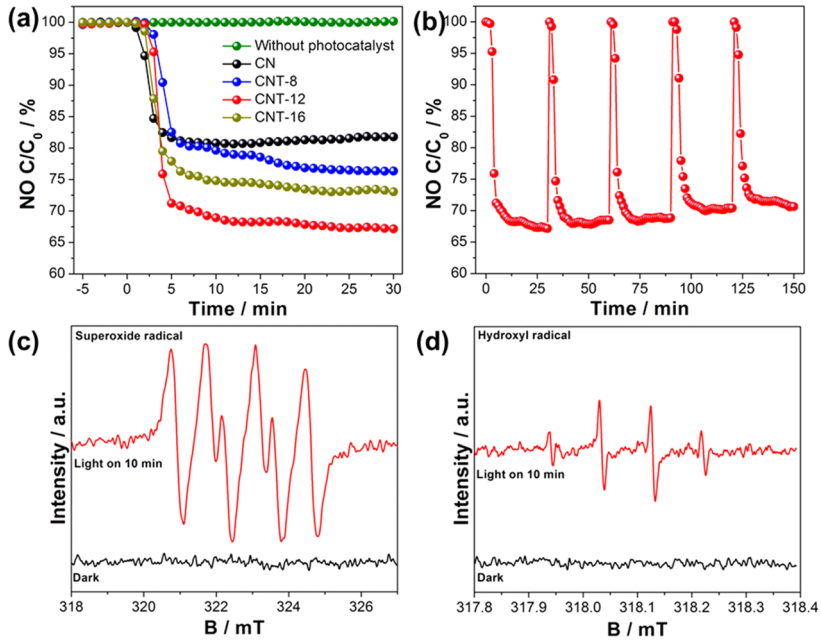

Figure 3. (a) Visible light photocatalytic activities of CN, CNT-8, CNT-12, and CNT-16 toward NO removal in air. (b) Cycling of CNT-12 during NO removal. (c) DMPO spin-trap ESR spectra of CNT-12 dispersed in (a) methanol for DMPO−$^{\bullet}O_2^-$ and (d) water for DMPO−$^{\bullet}$OH.

Information) was used to reveal its contribution during photocatalytic NO removal processes.[6] As shown in Figure S8, the value of η of CNT-12 was reduced from 32.8 to 21.3% after introducing KI, indicating that holes were also the active species for NO removal. These results indicate that $^{\bullet}O_2^-$ and h^+ are the dominant active species during NO oxidation over CNT-12 and that $^{\bullet}$OH radicals make minor contributions due to limited pathways for their generation.

Photocatalytic Activity Enhancement Mechanism. According to the ESR results, $^{\bullet}O_2^-$ radicals are crucial active species involved in the removal of NO. The formation of $^{\bullet}O_2^-$ involves two steps, namely, the adsorption of O_2 onto the surface of the material in the dark and the reduction of the adsorbed O_2 by photogenerated electrons upon irradiation with light. To investigate the differences in the O_2 adsorption behavior of g-C_3N_4 and N_{2c}-deficient g-C_3N_4 in detail, O_2 adsorption energies and EDDs were calculated by DFT; models of O_2 adsorbed on g-C_3N_4 and N_{2c}-deficient g-C_3N_4 following geometry optimization are shown in Figure 4a,b, respectively. From the perspective of thermodynamics,

DOI: 10.1021/acsami.8b21987
ACS Appl. Mater. Interfaces 2019, 11, 10651−10662

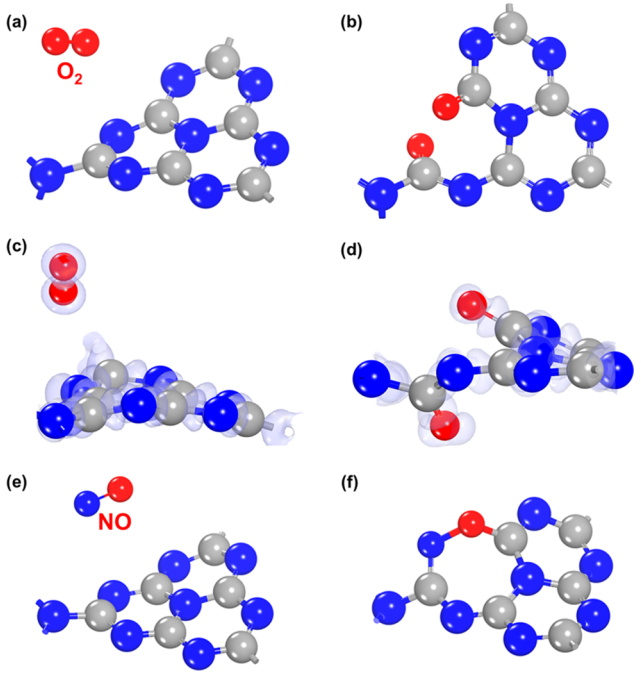

Figure 4. Models of O_2 adsorbed on: (a) g-C_3N_4 and (b) N-deficient g-C_3N_4 after geometry optimization. The corresponding calculated EDD diagrams of O_2 absorbed on: (c) g-C_3N_4 and (d) N-deficient g-C_3N_4. Models of NO adsorbed on: (e) g-C_3N_4 and (f) N-deficient g-C_3N_4 after geometry optimization.

molecular O_2 is difficult to adsorb onto unbroken g-C_3N_4 due to the positive ΔE_{ads} (0.48 eV). In contrast, it spontaneously adsorbs at the N_{2c}-deficient site because of the negative ΔE_{ads} (−5.99 eV). This chemisorption is accompanied by electron transfer between the absorbed O_2 and the g-C_3N_4, with electron coupling further promoting O_2 activation. To identify the degree of O_2 activation in g-C_3N_4 and N-deficient g-C_3N_4, the EDDs of the O_2-adsorbed models were calculated, which revealed that about 1.05 electrons are transferred from the N-deficient g-C_3N_4 to the O_2 (Figure 4d), but only 0.05 electrons are transferred from g-C_3N_4 to O_2 (Figure 4c). Furthermore, molecular O_2 eventually dissociates into two active O atoms at the N-vacancy site (Figure 4b); these active O atoms are easier to reduce to $^{\bullet}O_2^-$ than to molecular O_2 by photogenerated electrons. In addition, models of NO adsorbed on g-C_3N_4 and N-deficient g-C_3N_4 are shown in Figure 4e,f, respectively, with corresponding adsorption energies calculated. The calculations reveal that molecular NO is difficult to adsorb onto unbroken g-C_3N_4 (Figure 4e, ΔE_{ads} = 0.29 eV) but spontaneously adsorbs at the N_{2c}-deficient site (Figure 4f, ΔE_{ads} = −5.91 eV). These results indicate that N-vacancies not only increase the O_2 and NO adsorption capacities, but also realize the dissociative activation of molecular O_2, which decreases the barrier to the formation of $^{\bullet}O_2^-$ in subsequent photoreaction processes.

To illustrate changes in the photoelectric separation efficiency after N-vacancies are introduced into the tubular structure, transient photocurrents and PL spectra were recorded for pristine CN and CNT samples. Figure 5a reveals that the photocurrents generated by the CNT samples are generally higher than those of bulk CN, which suggests that the CNT samples have superior photoinduced charge-separating abilities owing to their hollow tubular structures with thinner layers (Figure S9).[59,60] In addition, the CNT samples possess similar hollow tubular structures. The photocurrent was observed to increase from an average value of 0.59 $\mu A/cm^2$ for CNT-8 to an average value of 1.12 $\mu A/cm^2$ for CNT-12 owing to the larger BET surface area of the latter, which provides more surface N-vacancies.[33,49] The photocurrent then decreases to an average value of 0.90 $\mu A/cm^2$ for CNT-16 owing to the excessive loss of ordered tri-*s*-triazine framework

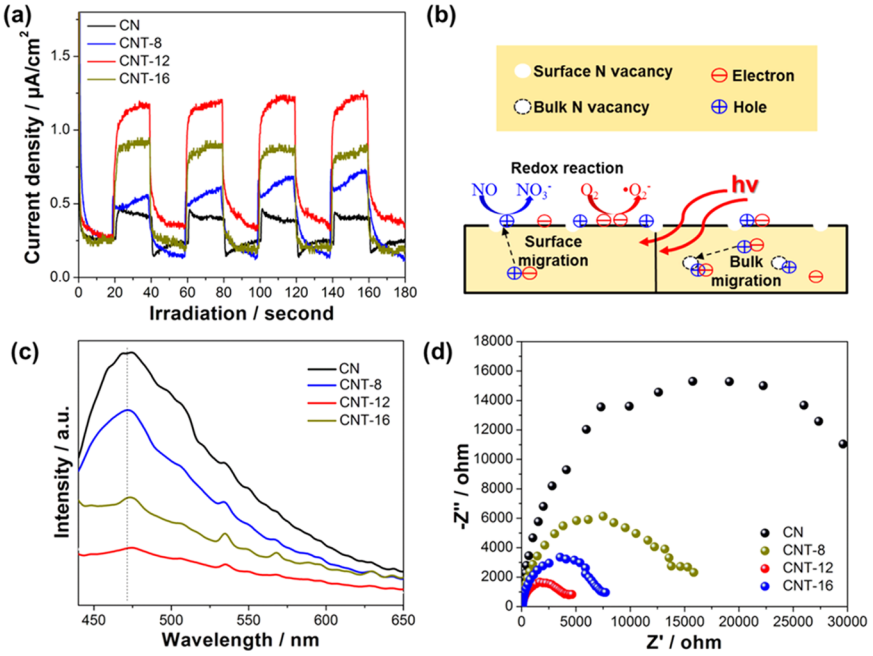

Figure 5. (a) Transient photocurrent responses of CN, CNT-8, CNT-12, and CNT-16. (b) Schematic diagram depicting the roles of N-vacancies in the migration and separation behavior of photoinduced charges and holes pairs. (c) PL spectra and (d) Nyquist plots of CN, CNT-8, CNT-12, and CNT-16.

DOI: 10.1021/acsami.8b21987
ACS Appl. Mater. Interfaces 2019, 11, 10651−10662

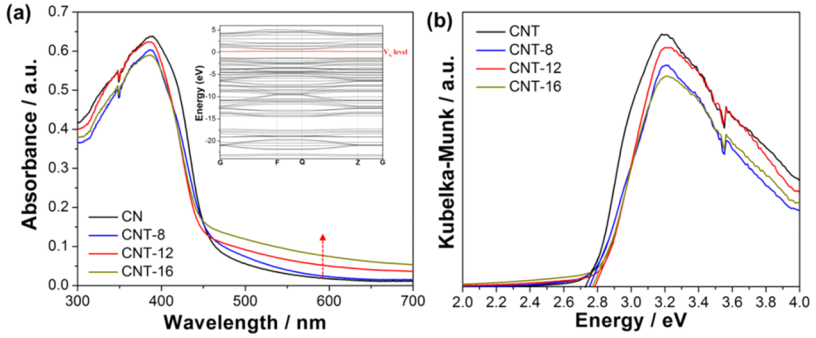

Figure 6. (a) UV−vis absorption spectra of CN, CNT-8, CNT-12, and CNT-16, and the calculated electronic structure (inset) of N-deficient g-C_3N_4. (b) Transformed Kubelka−Munk functions of light-absorbed CN, CNT-8, CNT-12, and CNT-16.

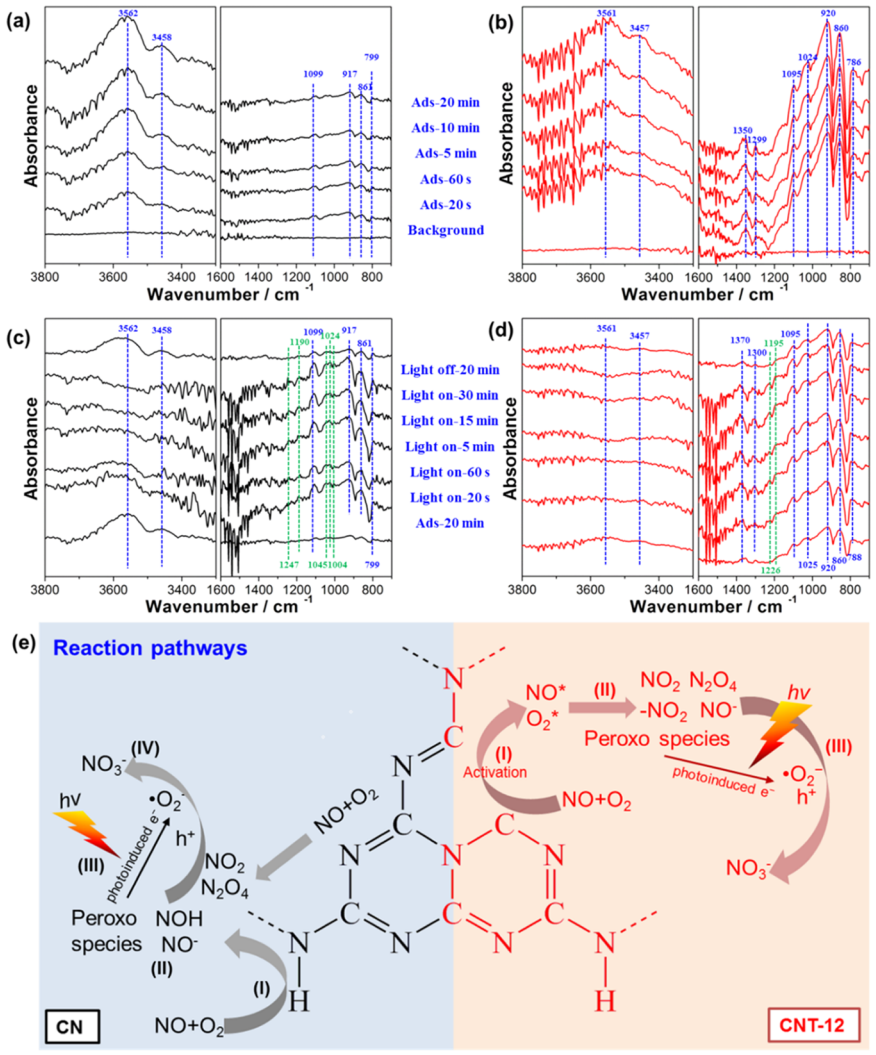

Figure 7. Time-dependent DRIFTS images for the adsorption of NO and O2, and their photocatalytic reactions on (a, c) CN and (b, d) CNT-12. (e) Depicting the proposed reaction pathways for adsorption and the photocatalytic oxidation of NO over pristine (left) and N-deficient (right) g-C_3N_4.

structures in CNT-16 and its very high concentration of bulk N-defects.[33,49] These results indicated that surface N-vacancies, as hole traps, are beneficial for reducing photo-induced charge-carrier recombination, leading to more charges and holes that migrate to the catalyst surface and take part in subsequent redox chemistry. However, N-vacancies in the bulk can provide similar pathways, which restrict charges and holes to the bulk and negatively affect the electrochemical response and photocatalytic activity (Figure 5b). Furthermore, as shown in Figure 5c, CNT-12 exhibits the lowest PL intensity and is ∼82% quenched relative to bulk CN, which further suggests that the recombination of photogenerated charges is more substantially suppressed in CNT-12 than in the other samples.

To further investigate the differences between the irregular bulk morphology and the tubular structure toward charge-transport capacity, these samples were subjected to EIS in the

DOI: 10.1021/acsami.8b21987
ACS Appl. Mater. Interfaces 2019, 11, 10651−10662

dark. Figure 5d reveals that the radii of the arcs in the Nyquist plots of the CNT samples are smaller than those of CN, indicating that 1D tubular structures facilitate facile charge-carrier transport in their longitudinal directions.[40,61] Among the tubular structures, CNT-12, with the smallest arc radius, exhibited the highest charge-transfer efficiency, owing to its suitable thin-wall construction and longitudinal structure; however, the performance of CNT-16, with a similar thin-wall structure, was unsatisfactory, which is ascribable to the loss of intralayer long-range ordered tri-*s*-triazine units (as evidenced by XRD; see Figure 1a). These above-mentioned results demonstrate that suitable surface N-vacancies and 1D tubular ordered structures are responsible for effective electron−hole separation and transfer, leading to enhanced photocatalytic activity.

Moreover, the optical absorbing abilities and band gaps of the prepared g-C_3N_4 samples were examined by UV−vis diffuse reflectance spectroscopy, the results of which are shown in Figure 6a. Compared to bulk CN, clear blue shifts in the intrinsic absorption edges, from 458 nm for CN to 451, 446, and 447 nm for CNT-8, CNT-12, and CNT-16 were observed, respectively, which are the result of increasingly thin layers that reduce interlayer electron coupling.[60] However, increased absorption tails are observed in the visible light regions of the spectra of the CNT samples that are due to N-defect states.[62] The electronic structures of g-C_3N_4 and N-deficient g-C_3N_4 were calculated based on the atomic structure models shown in Figure S1. Compared to the electronic structure of g-C_3N_4 (Figure S10), a defect energy level is observed for N-deficient g-C_3N_4, as illustrated in Figure 6a, which coincides with the increasing absorption tail observed for the CNT samples (Figure 6a). The band gaps were determined by the Kubelka−Munk method to be 2.71, 2.75, 2.78, and 2.77 eV for CN, CNT-8, CNT-12, and CNT-16, respectively (Figure 6b). The valence band (VB) and conduction band (CB) potentials of a semiconductor material can be determined using empirical equations, the details of which are provided in the Supporting Information; the positions of the VBs and CBs of the as-prepared samples were calculated to be 1.59 and −1.13 V for CN, 1.60 and −1.15 V for CNT-8, 1.62 and −1.16 V for CNT-12, and 1.62 and −1.15 V for CNT-16, respectively. Hence, N-vacancies simultaneously enhance the visible light-absorbing ability of g-C_3N_4, while slightly enhancing its redox capabilities.

Adsorption Sites, and the Identification of Intermediates and Photocatalytic Reaction Pathways. Based on the aforementioned DFT results for O_2 and NO adsorption, N-vacancies are proposed to be the active sites that adsorption-activate reactants. To further verify this hypothesis, the NO- and O_2-adsorption processes over CN and CNT-12 were investigated by in situ DRIFTS, the results of which are displayed in Figure 7a,b, respectively. A background spectrum was recorded after pretreating each sample with high-purity He; detailed descriptions of the NO- and O_2-adsorption processes over CN are provided in the Supporting Information, which revealed that both NO and O_2 adsorb at the N−H bonds of CN to form NOH and OOH bonds, respectively; NO^- and surface peroxo species are formed as a result of these activation processes. Compared to the adsorption reactions of CN (Figure 7a), some clear differences are observed when NO and O_2 are adsorbed by CNT-12. First, two new adsorption peaks were observed to gradually appear at 1350 and 1299 cm^{-1} in the spectra shown in Figure 7b; these peaks are assigned to adsorbed nitro compounds ($-NO_2$).[63,64] A DFT model of NO and O_2 co-adsorbed on N-deficient g-C_3N_4 was built and is displayed in Figure S11; this model reveals that one of the active O atoms of O_2 binds to the N atom of NO to form the $-NO_2$ group following geometry optimization. In addition, a bidentate-state stretching band at 1024 cm^{-1} was observed.[63,64] These results indicate that N-vacancies can indeed absorb and activate NO and O_2 molecules. In addition, the NO_2 (3604−3740 cm^{-1}), NO^- (1095 cm^{-1}), N_2O_4 (920 cm^{-1}), and surface peroxo (860 and 786 cm^{-1}) peaks in the spectrum of the CNT-12 surface are more obvious than those in the spectrum of the CN surface. However, the intensity of the NOH peak (3561 cm^{-1}) on the CNT-12 surface is weaker than that on the CN surface. These results indicate that NO and O_2 are more rapidly absorbed at N-vacancies through bidentate states than terminal N−H bonds due to extra active electrons.

Once adsorption equilibrium is established, a visible light source was applied to initiate photoreaction processes. Time-dependent DRIFTS images for the photocatalytic oxidation of NO over CN and CNT-12 are displayed in Figure 7c,d, respectively, with detailed descriptions of the photoreactions involving CN provided in the Supporting Information. Compared to the characteristic peaks of CN during photoreaction processes, new absorption bands were observed at 1500−1600 (monodentate nitrate, $\nu(NO_3)$), 1226 (bidentate nitrate, $\nu(NO_3)$), and 1192 (bidentate nitrite, $\nu(NO_2)$) cm^{-1}.[64] In addition, except for a slight decrease in the intensity of the 3562 cm^{-1} peak, peaks corresponding to other types of nitrates and peroxo species on the CNT-12 surface were more intense than those on the CN surface. These results demonstrate that the CNT-12 surface is more active than the CN surface during both adsorption and photocatalytic reaction phases. Notably, these new peaks almost disappear when the light was switched off after 20 min, with the adsorption equilibrium reestablished in both CN and CNT-12, consistent with NO_3^- dissociation.

Based on the aforementioned chain of evidence, we conclude that different reaction pathways and reactive sites are involved in the adsorption and photocatalytic oxidation of NO over pristine and N-deficient g-C_3N_4, as depicted in Figure 7e. Simply, NO and O_2 are absorbed at N−H bonds to form NOH and OOH bonds on pristine g-C_3N_4 (Figure 7e, left (I)), which are then activated to form NO^- and surface peroxo species (Figure 7e, left (II)) during adsorption. Upon illumination, the peroxo species are reduced by photogenerated electrons to form $^{\bullet}O_2^-$ (Figure 7e, left (III)) that, together with photogenerated h^+, oxidize absorbed-state intermediates to afford the end product (NO_3^-) (Figure 7e, left (IV)). However, NO and O_2 adsorption and photocatalysis over N-deficient g-C_3N_4 proceed via a different pathway. NO and O_2 are more rapidly absorbed at N-vacancies (Figure 7e, right (I)) through bidentate states, rather than at terminal N−H bonds; these species are activated and form nitro compounds ($-NO_2$) (Figure 7e, right (II)) rather than NOH or OOH bonds. Upon irradiation, the absorbed-state intermediates are oxidized to NO_3^- by $^{\bullet}O_2^-$ and h^+ at N-vacancies, as shown in Figure 7e, right (III).

CONCLUSIONS

In summary, in this study, we demonstrated a feasible method for the preparation of N-deficient g-C_3N_4 with a porous tubular micro-nanostructure that enhances O_2 activation, photo-induced charge-carrier separation, and oriented transfer. The

DOI: 10.1021/acsami.8b21987
ACS Appl. Mater. Interfaces 2019, 11, 10651−10662

optimal sample, CNT-12, exhibited a NO removal ratio under visible light irradiation that was 1.8 times higher than that of bulk g-C_3N_4. The spatial distribution of N-vacancies activates and dissociates molecular O_2 while also affecting electron-separation behavior. The porous tubular architecture favors the oriented transfer of charge carriers and the diffusion of reactants. These factors contribute to the observed enhancement in photocatalytic activity compared to the bulk material. in situ DRIFTS revealed that NO and O_2 participate in adsorption/photoreactions at N-vacancies in N-deficient g-C_3N_4 and at terminal N−H bonds in pristine g-C_3N_4. This study has established a feasible strategy for modifying g-C_3N_4 through simultaneous N-vacancy incorporation and morphology modulation, which improves photocatalytic activity toward NO_x degradation.

■ ASSOCIATED CONTENT

Supporting Information

The Supporting Information is available free of charge on the ACS Publications website at DOI: 10.1021/acsami.8b21987.

Structure models of g-C_3N_4 and N-deficient g-C_3N_4; element contents for M, M-8, M-12, M-16, CN, CNT-8, CNT-12, and CNT-16 samples; surface N/C atomic ratio, N_{2c}/N_{3c} area ratio of obtained g-C_3N_4 samples determined by XPS and bulk N/C atomic ratio of obtained precursors and g-C_3N_4 samples by elemental analyzer; XPS analysis of CNT-8, CNT-12, and CNT-16 samples; XPS analysis of oxygen concentration of CN, CNT-8, CNT-12, and CNT-16 samples; high-resolution O 1s XPS of CN, CNT-8, CNT-12, and CNT-16; SEM images of CN; TEM images of CNT-8 and CNT-16; SEM images of M, M-6, and M-7; XRD patterns of single melamine treated by different hydrothermal times (6, 7, 8, 12, and 16 h); schematic crystal structure of melamine and melamine−cyanuric acid supramolecular precursor; FT-IR spectra of single melamine treated by different hydrothermal times: 0, 6, 7, 8, 12, and 16 h and CA; reaction rate constants k of CN, CNT-8, CNT-12, and CNT-16; monitoring of the fraction of NO_2 in the outlet of the reactor and NO_2 selectivity of the CN, CNT-8, CNT-12, and CNT-16; visible light photocatalytic activities of CNT-12 toward NO removal in air with/without the addition of KI; photoinduced carrier separation processes in bulk and layered structure of g-C_3N_4; calculated electronic structures of g-C_3N_4; and DFT model of NO and O_2 co-adsorption on N-deficient g-C_3N_4 (PDF)

■ AUTHOR INFORMATION

Corresponding Author

*E-mail: huangyu@ieecas.cn. Tel: 86-29-6233 6261.

ORCID

Yu Huang: 0000-0003-3334-4849

Shun Cheng Lee: 0000-0001-5144-8372

Author Contributions

The manuscript was written through contributions of all authors. All authors have given approval to the final version of the manuscript.

Notes

The authors declare no competing financial interest.

■ ACKNOWLEDGMENTS

This research was financially supported by the National Key Research and Development Program of China (2016YFA0203000 and 2017YFC0212200) and the National Science Foundation of China (Nos. 41573138 and 51878644). Moreover, we acknowledge the partial support by the Key Research and Development Program of Shaanxi Province (No. 2018ZDCXL-SF-02-04). Y.H. was also supported by the "Hundred Talent Program" of the Chinese Academy of Sciences.

■ REFERENCES

(1) Gong, X.; Kaulfus, A.; Nair, U.; Jaffe, D. A. Quantifying O_3 Impacts in Urban Areas Due to Wildfires Using a Generalized Additive Model. *Environ. Sci. Technol.* **2017**, *51*, 13216−13223.

(2) Huang, R.-J.; Zhang, Y.; Bozzetti, C.; Ho, K.-F.; Cao, J.-J.; Han, Y.; Daellenbach, K. R.; Slowik, J. G.; Platt, S. M.; Canonaco, F.; Zotter, P.; Wolf, R.; Pieber, S. M.; Bruns, E. A.; Crippa, M.; Ciarelli, G.; Piazzalunga, A.; Schwikowski, M.; Abbaszade, G.; Schnelle-Kreis, J.; Zimmermann, R.; An, Z.; Szidat, S.; Baltensperger, U.; El Haddad, I.; Prevot, A. S. H. High Secondary Aerosol Contribution to Particulate Pollution during Haze Events in China. *Nature* **2014**, *514*, 218−222.

(3) Chen, H.; Nanayakkara, C. E.; Grassian, V. H. Titanium Dioxide Photocatalysis in Atmospheric Chemistry. *Chem. Rev.* **2012**, *112*, 5919−5948.

(4) Huang, Y.; Liang, Y.; Rao, Y.; Zhu, D.; Cao, J.-j.; Shen, Z.; Ho, W.; Lee, S. C. Environment-Friendly Carbon Quantum Dots/$ZnFe_2O_4$ Photocatalysts: Characterization, Biocompatibility, and Mechanisms for NO Removal. *Environ. Sci. Technol.* **2017**, *51*, 2924−2933.

(5) Wang, Z.; Yan, S.; Sun, Y.; Xiong, T.; Dong, F.; Zhang, W. Bi Metal Sphere/Graphene Oxide Nanohybrids with Enhanced Direct Plasmonic Photocatalysis. *Appl. Catal., B* **2017**, *214*, 148−157.

(6) Zhang, Q.; Huang, Y.; Peng, S.; Zhang, Y.; Shen, Z.; Cao, J.-j.; Ho, W.; Lee, S. C.; Pui, D. Y. H. Perovskite $LaFeO_3$-$SrTiO_3$ Composite for Synergistically Enhanced NO Removal Under Visible Light Excitation. *Appl. Catal., B* **2017**, *204*, 346−357.

(7) Fujiwara, K.; Mueller, U.; Pratsinis, S. E. Pd Subnano-Clusters on TiO_2 for Solar-Light Removal of NO. *ACS Catal.* **2016**, *6*, 1887−1893.

(8) Wang, W.; Huang, Y.; Zhang, X.; Cao, J. J.; Ho, W.; Lee, S. C. Three-Dimensional Bi_5O_7I Photocatalysts for Efficient Removal of NO in Air Under Visible Light. *Aerosol Sci. Eng.* **2017**, *1*, 33−40.

(9) Jia, Y.; Li, S.; Gao, J.; Zhu, G.; Zhang, F.; Shi, X.; Huang, Y.; Liu, C. Highly Efficient $(BiO)_2CO_3$-BiO_{2-x}-graphene Photocatalysts: Z-Scheme Photocatalytic Mechanism for Their Enhanced Photocatalytic Removal of NO. *Appl. Catal., B* **2019**, *240*, 241−252.

(10) Choi, C. H.; Lin, L.; Gim, S.; Lee, S.; Kim, H.; Wang, X.; Choi, W. Polymeric Carbon Nitride with Localized Aluminum Coordination Sites as a Durable and Efficient Photocatalyst for Visible Light Utilization. *ACS Catal.* **2018**, *8*, 4241−4256.

(11) Ong, W.-J.; Tan, L.-L.; Ng, Y. H.; Yong, S.-T.; Chai, S.-P. Graphitic Carbon Nitride (g-C_3N_4)-Based Photocatalysts for Artificial Photosynthesis and Environmental Remediation: Are We a Step Closer To Achieving Sustainability? *Chem. Rev.* **2016**, *116*, 7159−7329.

(12) Dong, G.; Yang, L.; Wang, F.; Zang, L.; Wang, C. Removal of Nitric Oxide through Visible Light Photocatalysis by g-C_3N_4 Modified with Perylene Imides. *ACS Catal.* **2016**, *6*, 6511−6519.

(13) Wang, X.; Maeda, K.; Thomas, A.; Takanabe, K.; Xin, G.; Carlsson, J. M.; Domen, K.; Antonietti, M. A Metal-free Polymeric Photocatalyst for Hydrogen Production from Water under Visible Light. *Nat. Mater.* **2009**, *8*, 76−80.

(14) Chen, P.; Xing, P.; Chen, Z.; Lin, H.; He, Y. Rapid and Energy-efficient Preparation of Boron Doped g-C_3N_4 with Excellent

Performance in Photocatalytic H_2-evolution. *Int. J. Hydrogen Energy* **2018**, *43*, 19984−19989.
(15) He, Y.; Zhang, L.; Teng, B.; Fan, M. New Application of Z-scheme Ag_3PO_4/g-C_3N_4 Composite in Converting CO_2 to Fuel. *Environ. Sci. Technol.* **2015**, *49*, 649−656.
(16) Shi, L.; Liang, L.; Wang, F.; Liu, M.; Chen, K.; Sun, K.; Zhang, N.; Sun, J. Higher Yield Urea-derived Polymeric Graphitic Carbon Nitride with Mesoporous Structure and Superior Visible-light-responsive Activity. *ACS Sustainable Chem. Eng.* **2015**, *3*, 3412−3419.
(17) Zou, Y.; Shi, J.-W.; Ma, D.; Fan, Z.; Cheng, L.; Sun, D.; Wang, Z.; Niu, C. WS_2/Graphitic Carbon Nitride Heterojunction Nanosheets Decorated with CdS Quantum Dots for Photocatalytic Hydrogen Production. *ChemSusChem* **2018**, *11*, 1187−1197.
(18) Wang, Z.; Huang, Y.; Chen, L.; Chen, M.; Cao, J.; Ho, W.; Lee, S. C. In situ g-C_3N_4 Self-sacrificial Synthesis of a g-C_3N_4/$LaCO_3OH$ Heterostructure with Strong Interfacial Charge Transfer and Separation for Photocatalytic NO Removal. *J. Mater. Chem. A* **2018**, *6*, 972−981.
(19) Cui, W.; Li, J.; Dong, F.; Sun, Y.; Jiang, G.; Cen, W.; Lee, S. C.; Wu, Z. Highly Efficient Performance and Conversion Pathway of Photocatalytic NO Oxidation on SrO-Clusters@Amorphous Carbon Nitride. *Environ. Sci. Technol.* **2017**, *51*, 10682−10690.
(20) Zhu, J.; Carabineiro, S. A. C.; Shan, D.; Faria, J. L.; Zhu, Y.; Figueiredo, J. L. Oxygen Activation Sites in Gold and Iron Catalysts Supported on Carbon Nitride and Activated Carbon. *J. Catal.* **2010**, *274*, 207−214.
(21) Hong, Z.; Shen, B.; Chen, Y.; Lin, B.; Gao, B. Enhancement of Photocatalytic H_2 Evolution over Nitrogen-deficient Graphitic Carbon Nitride. *J. Mater. Chem. A* **2013**, *1*, 11754−11761.
(22) Zou, Y.; Shi, J.-W.; Ma, D.; Fan, Z.; He, C.; Cheng, L.; Sun, D.; Li, J.; Wang, Z.; Niu, C. Efficient Spatial Charge Separation and Transfer in Ultrathin g-C_3N_4 Nanosheets Modified with Cu_2MoS_4 as a Noble Metal-free Co-catalyst for Superior Visible Light-driven Photocatalytic Water Splitting. *Catal. Sci. Technol.* **2018**, *8*, 3883−3893.
(23) Zou, Y.; Ma, D.; Sun, D.; Mao, S.; He, C.; Wang, Z.; Ji, X.; Shi, J.-W. Carbon Nanosheet Facilitated Charge Separation and Transfer between Molybdenum Carbide and Graphitic Carbon Nitride toward Efficient Photocatalytic H_2 Rroduction. *Appl. Surf. Sci.* **2019**, *473*, 91−101.
(24) Liu, Y.; Xiao, C.; Li, Z.; Xie, Y. Vacancy Engineering for Tuning Electron and Phonon Structures of Two-Dimensional Materials. *Adv. Energy Mater.* **2016**, *6*, No. 1600436.
(25) Gong, X.-Q.; Selloni, A.; Batzill, M.; Diebold, U. Steps on Anatase TiO_2(101). *Nat. Mater.* **2006**, *5*, 665−670.
(26) Liu, G.; Yang, H. G.; Wang, X.; Cheng, L.; Lu, H.; Wang, L.; Lu, G. Q.; Cheng, H.-M. Enhanced Photoactivity of Oxygen-Deficient Anatase TiO_2 Sheets with Dominant {001} Facets. *J. Phys. Chem. C* **2009**, *113*, 21784−21788.
(27) Liu, G.; Yin, L.-C.; Wang, J.; Niu, P.; Zhen, C.; Xie, Y.; Cheng, H.-M. A Red Anatase TiO_2 Photocatalyst for Solar Energy Conversion. *Energy Environ. Sci.* **2012**, *5*, 9603−9610.
(28) Chen, G.; Zhao, Y.; Fu, G.; Duchesne, P. N.; Gu, L.; Zheng, Y.; Weng, X.; Chen, M.; Zhang, P.; Pao, C.-W.; Lee, J.-F.; Zheng, N. Interfacial Effects in Iron-Nickel Hydroxide-Platinum Nanoparticles Enhance Catalytic Oxidation. *Science* **2014**, *344*, 495−499.
(29) Lu, Y.; Huang, Y.; Zhang, Y.; Cao, J.-j.; Li, H.; Bian, C.; Lee, S. C. Oxygen Vacancy Engineering of Bi_2O_3/$Bi_2O_2CO_3$ Heterojunctions: Implications of the Interfacial Charge Transfer, NO Adsorption and Removal. *Appl. Catal., B* **2018**, *231*, 357−367.
(30) Tay, Q.; Kanhere, P.; Ng, C. F.; Chen, S.; Chakraborty, S.; Huan, A. C. H.; Sum, T. C.; Ahuja, R.; Chen, Z. Defect Engineered g-C_3N_4 for Efficient Visible Light Photocatalytic Hydrogen Production. *Chem. Mater.* **2015**, *27*, 4930−4933.
(31) Wu, P.; Wang, J.; Zhao, J.; Guo, L.; Osterloh, F. E. Structure Defects in g-C_3N_4 Limit Visible Light Driven Hydrogen Evolution and Photovoltage. *J. Mater. Chem. A* **2014**, *2*, 20338−20344.
(32) Niu, P.; Liu, G.; Cheng, H.-M. Nitrogen Vacancy-Promoted Photocatalytic Activity of Graphitic Carbon Nitride. *J. Phys. Chem. C* **2012**, *116*, 11013−11018.
(33) Yu, H.; Shi, R.; Zhao, Y.; Bian, T.; Zhao, Y.; Zhou, C.; Waterhouse, G. I. N.; Wu, L.-Z.; Tung, C.-H.; Zhang, T. Alkali-Assisted Synthesis of Nitrogen Deficient Graphitic Carbon Nitride with Tunable Band Structures for Efficient Visible-Light-Driven Hydrogen Evolution. *Adv. Mater.* **2017**, *29*, No. 1605148.
(34) Wu, N.; Wang, J.; Tafen, D. N.; Wang, H.; Zheng, J.-G.; Lewis, J. P.; Liu, X.; Leonard, S. S.; Manivannan, A. Shape-Enhanced Photocatalytic Activity of Single-Crystalline Anatase TiO_2 (101) Nanobelts. *J. Am. Chem. Soc.* **2010**, *132*, 6679−6685.
(35) Mor, G. K.; Shankar, K.; Paulose, M.; Varghese, O. K.; Grimes, C. A. Use of Highly-ordered TiO_2 Nanotube Arrays in Dye-sensitized Solar Cells. *Nano Lett.* **2006**, *6*, 215−218.
(36) Jun, Y.-S.; Park, J.; Lee, S. U.; Thomas, A.; Hong, W. H.; Stucky, G. D. Three-Dimensional Macroscopic Assemblies of Low-Dimensional Carbon Nitrides for Enhanced Hydrogen Evolution. *Angew. Chem., Int. Ed.* **2013**, *52*, 11083−11087.
(37) Shalom, M.; Inal, S.; Fettkenhauer, C.; Neher, D.; Antonietti, M. Improving Carbon Nitride Photocatalysis by Supramolecular Preorganization of Monomers. *J. Am. Chem. Soc.* **2013**, *135*, 7118−7121.
(38) Wang, Z.; Chen, M.; Huang, Y.; Shi, X.; Zhang, Y.; Huang, T.; Cao, J.; Ho, W.; Lee, S. C. Self-assembly Synthesis of Boron-doped Graphitic Carbon Nitride Hollow Tubes for Enhanced Photocatalytic NO_x Removal Under Visible Light. *Appl. Catal., B* **2018**, *239*, 352−361.
(39) Guo, S.; Deng, Z.; Li, M.; Jiang, B.; Tian, C.; Pan, Q.; Fu, H. Phosphorus-Doped Carbon Nitride Tubes with a Layered Micro-nanostructure for Enhanced Visible-Light Photocatalytic Hydrogen Evolution. *Angew. Chem., Int. Ed.* **2016**, *55*, 1830−1834.
(40) Tong, Z.; Yang, D.; Sun, Y.; Nan, Y.; Jiang, Z. Tubular g-C_3N_4 Isotype Heterojunction: Enhanced Visible-Light Photocatalytic Activity through Cooperative Manipulation of Oriented Electron and Hole Transfer. *Small* **2016**, *12*, 4093−4101.
(41) Wang, Z.; Guan, W.; Sun, Y.; Dong, F.; Zhou, Y.; Ho, W.-K. Water-assisted Production of Honeycomb-like g-C_3N_4 with ultralong carrier lifetime and outstanding photocatalytic activity. *Nanoscale* **2015**, *7*, 2471−2479.
(42) Kresse, G.; Furthmüller, J. Efficient Iterative Schemes for ab Initio Total-energy Calculations Using a Plane-wave Basis Set. *Phys. Rev. B* **1996**, *54*, No. 11169.
(43) Kresse, G.; Joubert, D. From Ultrasoft Pseudopotentials to the Projector Augmented-wave Method. *Phys. Rev. B* **1999**, *59*, No. 1758.
(44) Perdew, J. P.; Burke, K.; Ernzerhof, M. Generalized Gradient Approximation Made Simple. *Phys. Rev. Lett.* **1996**, *77*, No. 3865.
(45) Blöchl, P. E. Projector Augmented-wave Method. *Phys. Rev. B* **1994**, *50*, No. 17953.
(46) Mulliken, R. S. Electronic Population Analysis on Lcao-mo Molecular Wave Functions.1. *J. Chem. Phys.* **1955**, *23*, 1833−1840.
(47) Chen, P.; Xing, P.; Chen, Z.; Hu, X.; Lin, H.; Zhao, L.; He, Y. In-situ Synthesis of $AgNbO_3$/g-C_3N_4 Photocatalyst via Microwave Heating Method for Efficiently Photocatalytic H_2 Generation. *J. Colloid Interface Sci.* **2019**, *534*, 163−171.
(48) Wang, Z.; Huang, Y.; Ho, W.; Cao, J.; Shen, Z.; Lee, S. C. Fabrication of $Bi_2O_2CO_3$/g-C_3N_4 Heterojunctions for Efficiently Photocatalytic NO in Air Removal: In-situ Self-sacrificial Synthesis, Characterizations and Mechanistic Study. *Appl. Catal., B* **2016**, *199*, 123−133.
(49) Niu, P.; Yin, L.-C.; Yang, Y.-Q.; Liu, G.; Cheng, H.-M. Increasing the Visible Light Absorption of Graphitic Carbon Nitride (Melon) Photocatalysts by Homogeneous Self-Modification with Nitrogen Vacancies. *Adv. Mater.* **2014**, *26*, 8046−8052.
(50) Shi, J.-W.; Zou, Y.; Ma, D.; Fan, Z.; Cheng, L.; Sun, D.; Wang, Z.; Niu, C.; Wang, L. Stable 1T-phase MoS_2 as an Effective Electron Mediator Promoting Photocatalytic Hydrogen Production. *Nanoscale* **2018**, *10*, 9292−9303.

DOI: 10.1021/acsami.8b21987
ACS Appl. Mater. Interfaces 2019, 11, 10651−10662

(51) Shi, L.; Liang, L.; Wang, F.; Liu, M.; Sun, J. Ag_2CrO_4 Nanoparticles Loaded on Two-dimensional Large Surface Area Graphite-like Carbon Nitride Sheets: Simple Synthesis and Excellent Photocatalytic Performance. *Dalton Trans.* **2016**, *45*, 5815−5824.
(52) Fu, J.; Zhu, B.; Jiang, C.; Cheng, B.; You, W.; Yu, J. Hierarchical Porous O-Doped g-C_3N_4 with Enhanced Photocatalytic CO_2 Reduction Activity. *Small* **2017**, *13*, No. 1603938.
(53) Shen, J.-S.; Cai, Q.-G.; Jiang, Y.-B.; Zhang, H.-W. Anion-triggered Melamine Based Self-assembly and Hydrogel. *Chem. Commun.* **2010**, *46*, 6786−6788.
(54) Jun, Y.-S.; Lee, E. Z.; Wang, X.; Hong, W. H.; Stucky, G. D.; Thomas, A. From Melamine-Cyanuric Acid Supramolecular Aggregates to Carbon Nitride Hollow Spheres. *Adv. Funct. Mater.* **2013**, *23*, 3661−3667.
(55) Shie, J.-L.; Lee, C.-H.; Chiou, C.-S.; Chang, C.-T.; Chang, C.-C.; Chang, C.-Y. Photodegradation Kinetics of Formaldehyde Using light sources of UVA, UVC and UVLED in the Presence of Composed Silver Titanium Oxide Photocatalyst. *J. Hazard. Mater.* **2008**, *155*, 164−172.
(56) Ai, Z.; Ho, W.; Lee, S.; Zhang, L. Efficient Photocatalytic Removal of NO in Indoor Air with Hierarchical Bismuth Oxybromide Nanoplate Microspheres under Visible Light. *Environ. Sci. Technol.* **2009**, *43*, 4143−4150.
(57) Chen, M.; Yao, J.; Huang, Y.; Gong, H.; Chu, W. Enhanced Photocatalytic Degradation of Ciprofloxacin over Bi_2O_3/$(BiO)_2CO_3$ Heterojunctions: Efficiency, Kinetics, Pathways, Mechanisms and Toxicity Evaluation. *Chem. Eng. J.* **2018**, *334*, 453−461.
(58) Ge, L.; Han, C.; Liu, J. Novel Visible Light-induced g-C_3N_4/Bi_2WO_6 composite photocatalysts for efficient degradation of methyl orange. *Appl. Catal., B* **2011**, *108*−*109*, 100−107.
(59) Liu, G.; Wang, T.; Zhang, H.; Meng, X.; Hao, D.; Chang, K.; Li, P.; Kako, T.; Ye, J. Nature-Inspired Environmental "Phosphorylation" Boosts Photocatalytic H_2 Production over Carbon Nitride Nanosheets under Visible-Light Irradiation. *Angew. Chem., Int. Ed.* **2015**, *54*, 13561−13565.
(60) Niu, P.; Zhang, L.; Liu, G.; Cheng, H.-M. Graphene-Like Carbon Nitride Nanosheets for Improved Photocatalytic Activities. *Adv. Funct. Mater.* **2012**, *22*, 4763−4770.
(61) Ran, J.; Ma, T. Y.; Gao, G.; Du, X.-W.; Qiao, S. Z. Porous P-doped Graphitic Carbon Nitride Nanosheets for Synergistically Enhanced Visible-light Photocatalytic H_2 Production. *Energy Environ. Sci.* **2015**, *8*, 3708−3717.
(62) Lu, L.; Wang, B.; Wang, S.; Shi, Z.; Yan, S.; Zou, Z. La_2O_3-Modified $LaTiO_2N$ Photocatalyst with Spatially Separated Active Sites Achieving Enhanced CO_2 Reduction. *Adv. Funct. Mater.* **2017**, *27*, No. 1702447.
(63) Kantcheva, M. Identification, Stability, and Reactivity of NO_x Species Adsorbed on Titania-supported Manganese Catalysts. *J. Catal.* **2001**, *204*, 479−494.
(64) Wu, J. C. S.; Cheng, Y. T. In situ FTIR study of Photocatalytic NO Reaction on Photocatalysts under UV Irradiation. *J. Catal.* **2006**, *237*, 393−404.

DOI: 10.1021/acsami.8b21987
ACS Appl. Mater. Interfaces 2019, 11, 10651−10662